Monthly Notices
of the
ROYAL ASTRONOMICAL SOCIETY

Mon. Not. R. Astron. Soc. **405,** 2317–2326 (2010) doi:10.1111/j.1365-2966.2010.16651.x

Observations from *Hinode*/EIS of intensity oscillations above a bright point: signature of the leakage of acoustic oscillations in the inner corona

A. K. Srivastava[1]★† and B. N. Dwivedi[2]★

[1]*Aryabhatta Research Institute of Observational Sciences (ARIES), Nainital-263129, India*
[2]*Department of Applied Physics, Institute of Technology, Banaras Hindu University, Varanasi-221005, India*

Accepted 2010 March 8. Received 2010 March 7; in original form 2009 May 28

ABSTRACT

We study the intensity oscillations in the upper chromosphere/transition region (TR) and corona, above a bright point (BP) in the solar atmosphere. We analyse the time series of He II 256 Å, Fe XII 195 Å and Fe XV 284 Å, observed in a 40-arcsec slot close to the centre of the Sun above the BP by the extreme ultraviolet (EUV) imaging spectrometer (EIS) on board *Hinode*. Using standard wavelet and periodogram tools, we produce power spectra of intensity oscillations. In the He II 256.32 Å and Fe XII 195.12 Å EUV light curves, we detect intensity oscillations of the periods $\sim$263 $\pm$ 80 s and $\sim$241 $\pm$ 60 s, respectively, with a probability >95 per cent in wavelets, which are also consistent with their periodograms. This provides the most likely signature of the propagation of acoustic oscillations around the $\sim$5.0-min period from the photosphere to the inner corona. The radiative cooling and thus the finite radiative relaxation time are found to be the most likely mechanisms for the reduced cut-off frequency environment above the observed BP. This may allow the transfer of $\sim$5.0-min acoustic oscillations from the upper chromosphere/TR into the corona. We find that intensity oscillations in He II 256.32 Å show temporal damping during the total span of the observation. This may be the first most likely observational signature of acoustic wave damping in the upper chromosphere caused by the radiative cooling effect. The intensity oscillations in Fe XII 195.12 Å show an amplification, which may be a most likely signature of the mode-coupling (two-wave interaction) and then resonant energy conversion, probably from transverse magnetohydrodynamic (MHD) waves of the double period (e.g. Alfvén waves) to the observed acoustic waves in the lower solar atmosphere where the plasma beta tends to unity. However, we find no evidence of real oscillations around the $\sim$5.0-min period with its amplification in the higher corona where the Fe XV 284.16 Å line is formed, which rules out this type of wave activity there. Almost 1.6 per cent of the solar surface is covered with small BPs, probably associated with the small-scale closed-loop system, which may be a subset of expanding flux tubes. Hence, the leakage of $\sim$5.0-min oscillations above such BPs, which is associated with the highest powers of strong convective motions, and probably resonantly amplified by transverse MHD waves (e.g. Alfvén waves), may be significant for heating the solar atmosphere locally.

Key words: MHD – waves – Sun: chromosphere – Sun: corona – Sun: oscillations – Sun: UV radiation.

1 INTRODUCTION

The understanding of coronal heating and the dynamics of transient events (e.g. coronal mass ejections, spicules, jets, surges, eruptive prominences, flares, etc.) is at the forefront of solar research. Two competing theories have been extensively investigated: one invokes magnetic reconnection and the other magnetohydrodynamic (MHD) waves. MHD waves (e.g. Alfvén, slow and fast magnetoacoustic waves) can transport the energy of powerful photospheric motions into the corona, leading to plasma heating. MHD waves can also power the transient events in the solar atmosphere. The magnetic reconnection can also be a potential candidate for plasma heating and the acceleration of solar transient events.

Recent ground-based and space-based observations show the presence of transverse waves (e.g. Cirtain et al. 2007; De Pontieu

★E-mail: aks@aries.res.in (AKS); bnd.app@itbhu.ac.in (BND)
†Send off-print request to Dr A. K. Srivastava, ARIES, Manora Peak, Nainital-263129, India.

et al. 2007; Erdélyi & Fedun 2007; Okamoto et al. 2007; Tomczyk et al. 2007; Jess et al. 2009; and references therein) and various types of magnetoacoustic waves (Erdélyi & Taroyan 2008; Gruszecki, Murawski & Ofman 2008; Ofman & Wang 2008; Srivastava et al. 2008a,b; Wang, Ofman & Davila 2009; Srivastava 2010; Srivastava & Dwivedi 2010, and references therein). However, the energy carried out by magnetoacoustic waves in the outer solar atmosphere is not sufficient either to heat the corona (Fossum & Carlsson 2005) or to accelerate the solar wind (Dwivedi & Srivastava 2008). Recently observed Alfvén waves, which are purely magnetic and incompressible in nature, may be a promising mechanism to explain the coronal heating and wind acceleration (Dwivedi & Srivastava 2006, and references therein). However, a few detections of Alfvén waves in the chromosphere and corona (e.g. Tomczyk et al. 2007) are still being debated. Instead, detected waves are suggested to be fast-mode kink waves, which also cause density perturbations (van Doorsselaere, Nakariakov & Verwichte 2008). Jess et al. (2009) have recently found an unambiguous presence of transverse Alfvén waves above bright points (BPs) in terms of FWHM oscillations of the Hα spectral line observed by the Swedish Tower Telescope (STT). This provides a unique opportunity to study the role of such waves in the chromosphere and corona. These waves may also be coupled with magnetoacoustic waves and can resonantly transfer energy in the region where the plasma beta approaches unity (Zaqarashvili & Roberts 2006; Zaqarashvili, Oliver & Ballester 2006). Thus, Alfvén waves penetrating in the upper solar atmosphere transfer energy to magnetoacoustic waves in the lower solar atmosphere.

Almost 1.6 per cent of the solar surface is covered with small BPs (e.g. Jess et al. 2009 and references cited there) probably associated with the small-scale closed-loop system, which may be a subset of expanding flux tubes. These BPs can support a variety of wave modes (e.g. Alfvén, fast and slow magnetoacoustic waves). In this paper, we study intensity oscillations from the upper chromosphere/transition region (TR) to the corona above a BP, which may likely be generated by resonant energy transfer from transverse MHD waves (e.g. Alfvén waves) to ∼5.0-min magnetoacoustic oscillations. We present our observations and data reduction in Section 2, and wavelet and periodogram analyses in Section 3. In Section 4, we give our results and discussion.

2 OBSERVATION AND DATA REDUCTION

We use time-series data of the on-disc BP system as observed in a 40-arcsec slot of the extreme ultraviolet (EUV) imaging spectrometer (EIS; Culhane et al. 2006). The 40- and 266-arcsec slots are appropriate for image analyses using light curves, while the 1- and 2-arcsec slits are ideal for spectral and Doppler analyses using spectral-line profiles. The EIS observes high-resolution spectra in two wavelength intervals, 170–211 and 246–292 Å, using short-wavelength (SW) and long-wavelength (LW) CCDs, respectively. The spectral resolution of the EIS is 0.0223 Å per pixel. Observations were acquired on 2007 November 27, and the data contain images of Fe XIII 202.04 Å, Fe XI 188.23 Å, Si X 258.37 Å, Fe VIII 185.62 Å, Mg VII 280.75 Å, Fe XV 284.16 Å, Fe XIV 264.78 Å, Fe XII 195.12 Å, Si X 261.04 Å, Fe X 184.54 Å, Si VII 275.35 Å, Ca XVII 192.82 Å, He II 256.32 Å, and Fe XIV 274.20 Å. The observation started at 17:00:28 UT and ended at 17:27:01 UT. The full-disc *Hinode*/X-ray Telescope (XRT) image shows the pointing position (i.e. $X_{\rm CEN} = -5.62$ arcsec and $Y_{\rm CEN} = -226.21$ arcsec) and a full field of view ($X_{\rm FOV} = 40$ arcsec and $Y_{\rm FOV} = 512$ arcsec) of the 40-arcsec slot at 17:00:28 UT (Fig. 1). The binning of the data was 1×1 arcsec^2. The observation window on the CCDs is with

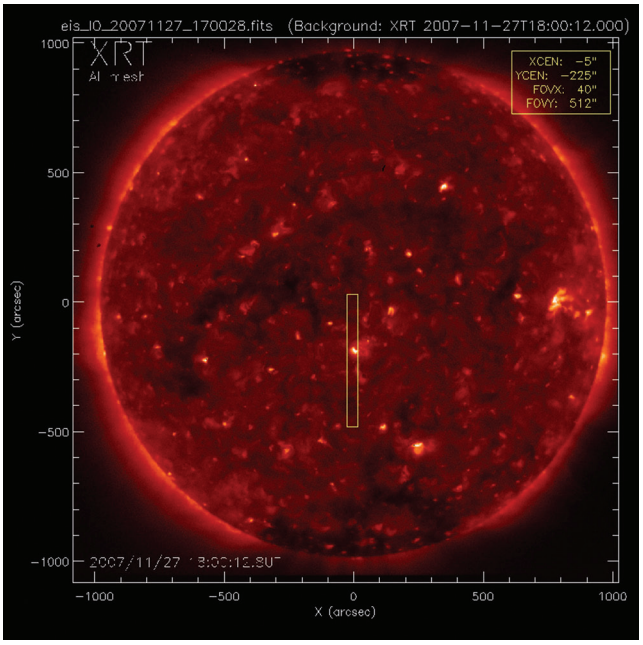

Figure 1. Full-disc *Hinode*/XRT image shows the pointing position (i.e. $X_{\rm CEN} \approx -5.0$ arcsec and $Y_{\rm CEN} \approx -225.0$ arcsec) and full field of view ($X_{\rm FOV} = 40$ arcsec and $Y_{\rm FOV} = 512$ arcsec) of the 40-arcsec slot. (Credit: The Hinode Team and the Hinode EIS data archive at UCL-Mullard Space Science Laboratory.)

a height of 512 pixels along the slot, and a width of 40 pixels in the wavelength direction, which is the direction of the dispersion by spectral resolution of 0.0222 Å. The average size of the spatial X-step (0.1 arcsec pixel^{-1}) in the horizontal direction was equal to one time-step in the same direction (∼32 s per step) during the sit-n-stare observations of the BP. The total span of the X-spatial steps in the horizontal direction was between −3 to −8 arcsec, while the total time-span of the sit n stare was ∼26.6 min. The exposure time for the observation was ∼32 s, and the integration time for each step of the time series was uniform, being ∼32 s.

We acquire a time-series observation of a BP using the 40-arcsec slot of the *Hinode*/EIS. In the time-series observations, the wide slot has been pointed with a 48-pixel width (X_λ) in the wavelength dispersion direction with a spectral resolution of 0.0222 Å pixel^{-1}, and the height of the slot (Y) was 512 pixels with a spatial scale of 1 arcsec pixel^{-1}. While acquiring the time series, the pointed slot (see Fig. 1) moves, tracking the BP between 17:00:28.000 and 17:26:30.797 UT on 2007 November 27 with full time-steps of 50 (i.e. ∼31.8 s per step). The equivalent horizontal steps ($X_{\rm SUN}$; i.e. a total of 50 steps) have been carried out in the solar X-direction, covering $X_{\rm SUN} = -7.63191$ arcsec east to $X_{\rm SUN} = -3.61481$ arcsec east. It should be noted that the correlation tracker was on during this sit-n-stare (time-series) observation. Similarly, the total vertical space is covered from $Y_{\rm SUN} = 29.2888$ arcsec north to $Y_{\rm SUN} = -481.711$ arcsec south along with each horizontal distance and time-step of the sit-n-stare observation. We apply standard EIS data-reduction procedures to the data acquired at the telescope [the raw (zeroth-level) data]. The subroutines can be found in the SSWIDL software tree.[1] These standard subroutines correct for dark-current subtraction, cosmic-ray removal, flat-field correction, hot pixels, warm pixels and bad/missing pixels. The data are saved in

[1] http://www.darts.isas.jaxa.jp/pub/solar/ssw/hinode/eis/

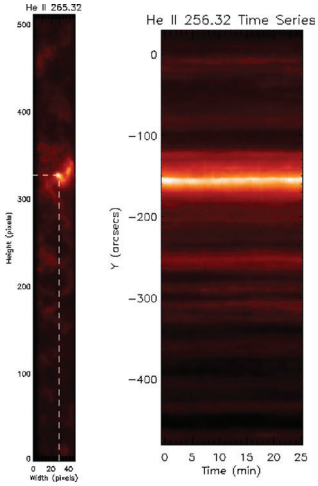

Figure 2. He II 256.32 image slice at 17:00:28 UT on 2007 November 27 (left panel) shows the 512-pixel full vertical window height ($Y_{\rm SUN}$ = 1 arcsec pixel^{-1}) and 48-pixel window width in the direction of wavelength dispersion (X_λ = 0.0222 Å pixel^{-1}). The brightest core of the BP is selected as (X_λ, $Y_{\rm SUN}$) ∼ [28.89th pixel, 327.03th pixel (or −154.711 arcsec)] as observed by the LW CCD independently. The corresponding temporal image data are shown in the right panel where $Y_{\rm SUN}$ is expressed in arcsec while the X-axis is labelled in time (min). The temporal variation of the intensity (in DN units) of the BP core (left panel) is shown in the right panel at $Y_{\rm SUN}$ = −154.711 arcsec. The He II 256.32 Å image is considered as a reference to co-align the coronal images.

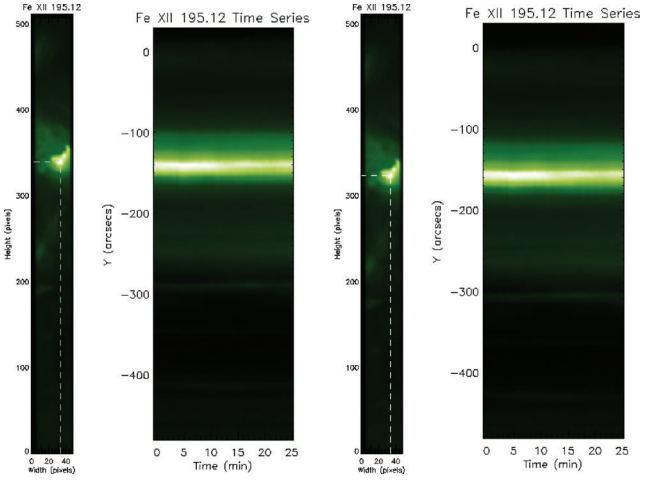

Figure 3. Fe XII 195.12 image slice on 17:00:28 UT (leftmost), which shows the 512-pixel full vertical window height ($Y_{\rm SUN}$ = 1 arcsec pixel^{-1}) and 48-pixel window width in the direction of wavelength dispersion (X_λ = 0.0222 Å pixel^{-1}). The brightest core of the BP is at (X_λ, $Y_{\rm SUN-OLD}$) ∼ [33.89th pixel, 339.04th pixel (or −142.711 arcsec)] as observed by the SW CCD independently (leftmost panel). The corresponding temporal image data are shown in the middle-left panel where $Y_{\rm SUN-OLD}$ is expressed in arcsec while the X-axis is labelled in time (min). The temporal variation of the intensity (in DN units) of the BP core (leftmost panel) is shown in the middle-left panel at $Y_{\rm SUN-OLD}$ = −142.711 arcsec. The same BP core is acquired at (X_λ, $Y_{\rm SUN-NEW}$) ∼ [33.89th pixel, 322.832th pixel (or −159.711 arcsec)] after its co-alignment with the He II 256.32 Å image as observed by the LW CCD (middle-right panel). The corresponding temporal image data are shown in the rightmost panel where $Y_{\rm SUN-NEW}$ is expressed in arcsec and the X-axis is labelled in time (min). The temporal variation of intensity (in DN units) of the same BP core (middle-right panel) is shown in the rightmost panel at $Y_{\rm SUN-NEW}$ = −159.711 arcsec.

the level-1 data file, while associated errors are saved in the error file. Because we analyse the nature of oscillations in the BP system from the chromosphere to the high-temperature corona, we choose three lines, He II 256.12 Å (upper chormospheric/TR), Fe XII 195.12 Å (coronal) and Fe XV 284.16 Å (upper coronal line suitable to capture the activity of the region), with enough signal-to-noise (S/N) ratios to produce power spectra of their temporal image data. The summation of X or Y pixels was not completed to prevent information losses about the BP system in the on-disc BP. The subarcsec jitters also affect various EIS observations in different ways. However, these subarcsec jitters have no effect on the temporal image data in some cases (e.g. O'Shea & Doyle 2009; Srivastava & Dwivedi 2010). We have used the standard cross-correlation technique to remove the jitter effect from the temporal image data of He II 256.32 Å, Fe XII 195.12 Å and Fe XV 284.12 Å.

Fig. 2 displays the He II 256.32 Å image slice at 17:00:28 UT (left panel), which shows the 512-pixel full vertical window height ($Y_{\rm SUN}$ = 1 arcsec pixel^{-1}) and 48-pixel window width in the direction of wavelength dispersion (X_λ = 0.0222 Å pixel^{-1}). The brightest core of the BP is selected as (X_λ, $Y_{\rm SUN}$) ∼ [28.89th pixel, 327.03th pixel (or −154.711 arcsec)]. The corresponding temporal image data are shown in the right panel, where $Y_{\rm SUN}$ is expressed in arcsec and the X-axis is labelled in time (min). The temporal variation of the intensity (in DN units) of the BP core (left panel) is shown in the right panel at $Y_{\rm SUN}$ = −154.711 arcsec. The He II 256.32 Å image is considered as a reference to co-align the coronal images. We have chosen the brightened core of the BP lying in the upper chromosphere/TR at (X_λ, $Y_{\rm SUN}$) ∼ [28.89th pixel, 327.03th pixel (or −154.711 arcsec)]. We extract the EUV light curve from this location in the temporal image data of He II 256.32 Å for power spectral analyses. We find significant periodicity around ∼5.0 min (see $Y_{\rm SUN}$ = −154.711 arcsec related to the upper chromospheric/TR counterpart of the BP core in the right panel of Fig. 2.)

We have calculated the exact offset between the reference wavelength He II 256.32 Å and Fe XII 195.12 Å using the standard EIS subroutine, which is −16.2080 pixel (or −16.2080 arcsec) as $Y_{\rm SUN}$ is 1 arcsec pixel^{-1}. Fig. 3 shows the Fe XII 195.12 Å image slice at 17:00:28 UT (left panel), which shows the 512-pixel full vertical window height ($Y_{\rm SUN}$ = 1 arcsec pixel^{-1}) and 48-pixel window width in the direction of wavelength dispersion (X_λ = 0.0222 Å pixel^{-1}). The brightest core of the BP is at (X_λ, $Y_{\rm SUN-OLD}$) ∼ [33.89th pixel, 339.04th pixel (or −142.711 arcsec)] as observed by the SW CCD independently (left panel). The corresponding temporal image data are shown in the middle-left panel where $Y_{\rm SUN-OLD}$ is expressed in arcsec while the X-axis is labelled in time (min). The temporal variation of intensity (in DN units) of the BP core (left panel) is shown in the middle-left panel at $Y_{\rm SUN-OLD}$ = −142.711 arcsec. The same BP core is acquired at (X_λ, $Y_{\rm SUN-NEW}$) ∼ [33.89th pixel, 322.832th pixel (or −159.711 arcsec)] after its co-alignment with the He II 256.32 Å image as observed by the LW CCD (middle-right panel). The corresponding temporal image data are shown in the right panel where $Y_{\rm SUN-NEW}$ is expressed in arcsec while the X-axis is labelled in time (min). The temporal variation of intensity (in DN units) of the same BP core (middle-right panel) is shown in the right panel at $Y_{\rm SUN-NEW}$ = −159.711 arcsec.

We have also calculated the exact offset between the reference wavelength He II 256.32 Å and Fe XV 284.16 Å using the standard EIS subroutine, which is −2.20493 pixels (or −2.20493 arcsec) as $Y_{\rm SUN}$ is 1 arcsec pixel^{-1}. Fig. 4 shows the Fe XV 284.16 Å image slice on 17:00:28 UT (left panel), which shows the 512-pixel full vertical window height ($Y_{\rm SUN}$ = 1 arcsec pixel^{-1}) and 48-pixel window

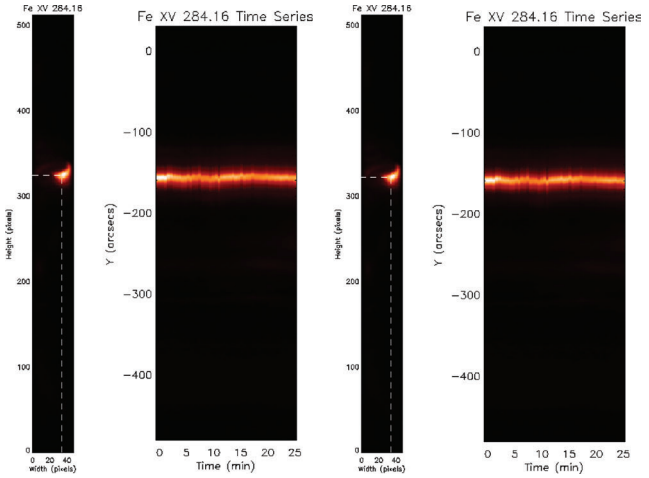

Figure 4. Fe XV 284.16 image slice at 17:00:28 UT (leftmost panel), which shows the 512-pixel full vertical window height ($Y_{\rm SUN} = 1$ arcsec pixel^{-1}) and 48-pixel window width in the direction of wavelength dispersion ($X_\lambda = 0.0222$ Å pixel^{-1}). The brightest core of the BP is at $(X_\lambda, Y_{\rm SUN-OLD}) \sim$ [34th pixel, 324th pixel (or -157.711 arcsec)] as observed by the LW CCD independently (leftmost panel). The corresponding temporal image data are shown in the middle-left panel where $Y_{\rm SUN-OLD}$ is expressed in arcsec while the X-axis is labelled in time (min). The temporal variation of intensity (in DN units) of the BP core (leftmost panel) is shown in the middle-left panel at $Y_{\rm SUN-OLD} = -157.711$ arcsec. The same BP core is acquired at $(X_\lambda, Y_{\rm SUN-NEW}) \sim$ [34th pixel, 321.835th pixel (or -160.711 arcsec)] after its co-alignment with the He II 256.32 Å image as observed by the LW CCD (middle-right panel). The corresponding temporal image data are shown in the rightmost panel where $Y_{\rm SUN-NEW}$ is expressed in arcsec and the X-axis is labelled in time (min). The temporal variation of intensity (in DN units) of the same BP core (middle-right panel) is shown in the rightmost panel at $Y_{\rm SUN-NEW} = -160.711$ arcsec.

width in the direction of wavelength dispersion ($X_\lambda = 0.0222$ Å pixel^{-1}). The brightest core of the BP is at $(X_\lambda, Y_{\rm SUN-OLD}) \sim$ [34th pixel, 324th pixel (or -157.711 arcsec)] as observed by the LW CCD independently (left panel). The corresponding temporal image data are shown in the middle-left panel where $Y_{\rm SUN-OLD}$ is expressed in arcsec while the X-axis is labelled in time (min). The temporal variation of intensity (in DN units) of the BP core (left panel) is shown in the middle-left panel at $Y_{\rm SUN-OLD} = -157.711$ arcsec. The same BP core is acquired at $(X_\lambda, Y_{\rm SUN-NEW}) \sim$ [34th pixel, 321.835th pixel (or -160.711 arcsec)] after its co-alignment with the He II 256.32 Å image as observed by the LW CCD (middle-right panel). The corresponding temporal image data are shown in the right panel where $Y_{\rm SUN-NEW}$ is expressed in arcsec while the X-axis is labelled in time (min). The temporal variation of intensity (in DN units) of the same BP core (middle-right panel) is shown in the right panel at $Y_{\rm SUN-NEW} = -160.711$ arcsec.

The top-left and top-right panels of Fig. 5 show the He II 256.32 Å intensity maps of the BP system, overplotted with the co-aligned Fe XII 195.12 Å and Fe XV 284.16 Å intensity contours, respectively. The locations of the brightest core of the BP system are indicated for both coronal lines. This location is around $Y_{\rm SUN-NEW} \sim -160$ arcsec, which probably indicates the coronal part of the associated flux-tube system. The bottom-left and bottom-right panels of Fig. 5 show the Fe XII 195.12 Å and Fe XV 195.12 Å intensity maps of the BP system, respectively, which are overplotted with the co-aligned He II 256.32 Å intensity contours. The upper chromospheric/TR counterpart locations of the brightest core of the BP system are indicated in these maps by He II 256.32 Å intensity contours. The

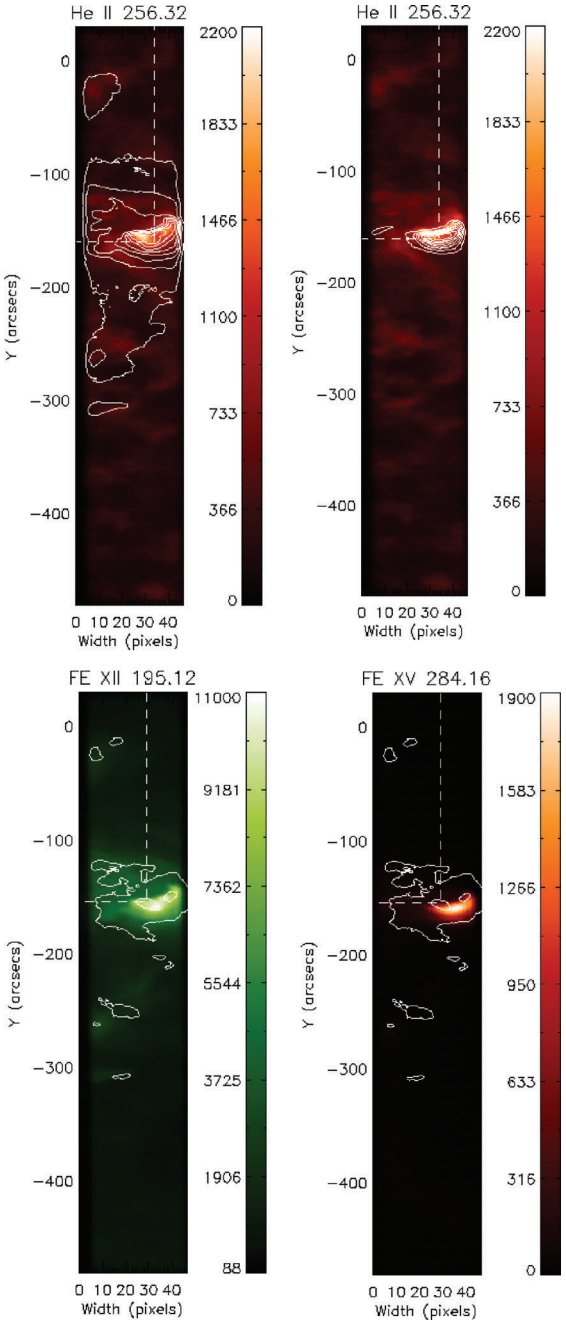

Figure 5. The top-left and right panels show the He II 256.32 Å intensity map of the BP system, respectively overplotted with the co-aligned Fe XII 195.12 Å and Fe XV 195.12 Å intensity contours. The locations of the brightest core of the BP are indicated in both coronal wavelengths. This point is $Y_{\rm SUN-NEW} \sim -160$ arcsec, and probably indicates the coronal part of the associated flux-tube system. The bottom-left and right panels show the Fe XII 195.12 Å and Fe XV 195.12 Å intensity maps of the BP system, respectively, which are overplotted with the co-aligned He II 256.32 Å intensity contours. The locations of the brightest core of the BP are indicated in the chromospheric/TR part of the BP system as visible in He II 256.32 Å. The two intense and singular contours probably show the footpoints (or lower ends) of the flux tube of the BP system, in which the western one is at $Y_{\rm SUN-NEW} \sim -154.711$ arcsec. The co-aligned images reveal the presence of a small-scale loop system, which may be a subset of the expanding flux-tube system of the BP. The footpoint traces (or lower ends) of the flux-tube system lie in the chromosphere/TR, while its apex (or upper end) lies in the corona. The colour bar is the strength of counts in DN units.

two intense and singular contours probably show the footpoints (or lower ends) of the flux tube of the BP system, in which the western one is at $Y_{\rm SUN-NEW} \sim -154.711$ arcsec. The co-aligned images reveal the presence of a small-scale loop system, which may be a subset of the expanding flux-tube system of the BP. The footpoint traces (or lower ends) of the flux-tube system lie in the chromosphere/TR, while its apex (or upper end) is in the corona and is visible in the coronal images. The colour bar is the strength of counts in DN units. The BP is probably expanded ∼10 arcsec in the corona, and thus the locations of brightest core in both coronal lines are accompanied by approximately the same location around $Y_{\rm SUN-NEW} \sim -160$ arcsec.

3 WAVELET AND PERIODOGRAM ANALYSES

We have used the wavelet analysis IDL code RANDOMLET developed by E. O'Shea. This program executes a randomization test (Linnell-Nemec & Nemec 1985; O'Shea et al. 2001), which is an additional feature along with the standard wavelet analysis code (Torrence & Compo 1998) to examine the statistically significant real periodicities in the time-series data. This test is distribution-free or non-parametric (i.e. it is not constrained by any specific noise model such as Poisson, Gaussian, etc.). Using this technique, many important results have already been published by analysing approximately evenly sampled data in the solar context (O'Shea et al. 2007; Srivastava et al. 2008a,b; O'Shea & Doyle 2009; Srivastava & Dwivedi 2010; Srivastava 2010), in the context of active galactic nuclei (Gupta, Srivastava & Wiita 2009), and in the stellar context (Pandey & Srivastava 2009).

Using wavelet analysis, the search for periodicities in EUV light curves is carried out by a time-localized function, which is continuous in both frequency and time. The Morlet wavelet function is used, which is defined as

$$\psi_t(s) = \pi^{-1/4} \exp(\mathrm{i}\omega t) \exp\left(\frac{-t^2}{2s^2}\right). \quad (1)$$

Here, t, s, ω and $\pi^{-1/4}$ are time, wavelet scale, oscillation frequency and the normalization constant, respectively. The Morlet function is the sine wavefunction modified by the Gaussian envelope. In the Morlet function, the Fourier period P is related to the wavelet scale s by the relation $P = 1.03$ s. The wavelet is convolved with the time series to determine the contribution of the frequency to time series, which matches the sinusoidal portion by varying the scale of the wavelet function. This method produces the power spectrum of the oscillations in different light curves. We note that the Morlet wavelet suffers from an 'edge effect' that is typical for analyses of time-series data. However, this effect is significant only in regions lying within a cone of influence (COI), which marks where possible periods, too close to either the measurement interval or the maximum length of the time series, cannot be convincingly detected.

The RANDOMLET software obtains measurements of the peak power in the global wavelet spectrum, which is the average peak power over time, and is equivalent to a smoothed Fourier power spectrum. The probability measurements of the real power peaks have been carried out by the randomization test of O'Shea et al. (2001). This technique parametrically estimates the fraction of permutations that provide peak values greater than or equal to the original peak power of the time series, which provides the probability (p) of the null periodic component. Thus, the acceptance percentage probability that real periodic components are present in the data is $(1-p)\times 100$. The details of the randomization test are given by Linnell-Nemec & Nemec (1985) and O'Shea et al. (2001). We have performed a running average of the raw data with the window widths '10' and '8', respectively, for the He II 256.32 Å and Fe XII 195.12 Å light curves. The running average almost exactly fits the long-term variations of raw data, which are subtracted before the power spectral analyses. It should be noted that the boxcar smoothing with a window of width T may tend to suppress the appearance of waves with periods that are integer multiples of T in the trend that is calculated. However, the COI of the data lies at ∼9.0 min and the EUV light curves that interest us contain long-term variations around the COI, which are unworthy and not globally distributed. Moreover, we could not find the globally distributed, statistically significant period below the COI other than the real periods around 5.0 min. This means that most of the longer periodicities may be a result of long-term variations, or closely associated with these. Therefore, we exactly fit these long-term variations to subtract them from the original light curves before wavelet and periodogram analyses. In general, the choice of window width in the running average of the time-series data should be made with caution, and also be re-examined by other alternative methods, as we have done in our analyses. The long-term trends lie in the He II 256.32 Å and Fe XII 195.12 Å EUV light curves and generate the power peaks mostly around the COI in their intensity wavelet spectra as well as global wavelet spectra. Moreover, they do not repeat even one cycle of periodicity over the total span of the time-series data. This may cause overimposition of such longer but unworthy periodicity related to the background trends over the statistically significant real power peaks lying below the COI in their power spectra. Such long-term background trends are typical of many solar observations, and thus the removal of these trends must be performed strictly in the search for real periodicities in temporal image/spectral data (e.g. Srivastava et al. 2008a,b; O'Shea & Doyle 2009, and references therein). There are several ways to remove such long-term trends (e.g. running average subtraction, polynomial fit of the trends and their subtraction, wavelet reconstruction at shorter Fourier scales from such long period trends, etc.). However, the use of one of these methods depends upon the nature of the trend presented in the light curves. In the case of the He II 256.32 Å EUV light curve, the background long-term trend seems to be decreasing over the total lifespan of the time-series data. This is the simplest behaviour of the trend, which can be easily fit by both 'running average' as well as 'low-order polynomial fit'. We have first fitted this trend by a running average of the scalar window of '10' (i.e. 5.3 min), which is then subtracted from the original time series. We have carried out wavelet and periodogram analyses on this detrended light curve, and obtained the statistically significant and globally distributed (>3 cycle) periodicity 263 ± 80 s (around 5.0 min) with a probability of 99–100 per cent in the intensity oscillations. Then, we have fitted this simpler trend again by a third-order polynomial fit, which also approximately fits the trend exactly. We have again examined the wavelet analysis of the detrended light curve by a polynomial fit, and obtained the same periodicity of 263 ± 80 s (around 5.0 min) in the He II 256.32 Å EUV light curve with the probability of 97 per cent in the intensity oscillations, which is still significant. However, the long-term trend of Fe XII 195.12 Å is approximately sinusoidal and exhibits approximately one cycle over the total lifespan of the time series. It is clear from the wavelet analysis, and also by viewing the long-term trend, that the power peak related to this trend lies above the COI in the intensity and global power spectra of Fe XII 195.12 Å. Hence, the low-order polynomial fitting is not appropriate to fit this long-term trend. In this case, we use the running average by window width of '8' (4.2 min) to approximately fit the background trend of the data. After

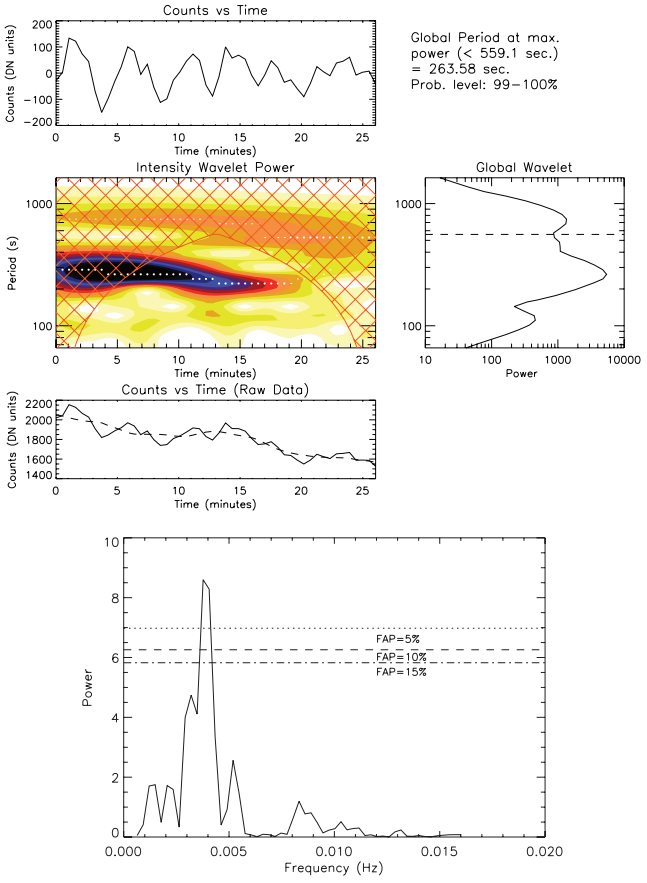

Figure 6. (a) The wavelet result for the He II 256.32 Å EUV light curve. The top panel shows the variation of intensity. The wavelet power spectrum is given in the middle-left panel, and the global power spectrum is given in the middle-right panel with the dotted line showing the maximum allowable period outside the COI. The light curve is extracted from the core of the most brightened part of the BP (lower end of the flux tube) $(X_\lambda, Y_{\rm SUN}) \sim$ [28.89th pixel, 327.03th pixel (or −154.711 arcsec)] as observed by the LW CCD independently, and detrended by a window width of 10 data points (i.e. ∼5.3 min) running average, which almost fit the long-term trend presented in the observed light curve. (b) The periodogram power spectrum of running average detrended light curve is presented in the bottom panel, which is consistent with the wavelet. The FAP levels are shown by horizontal lines.

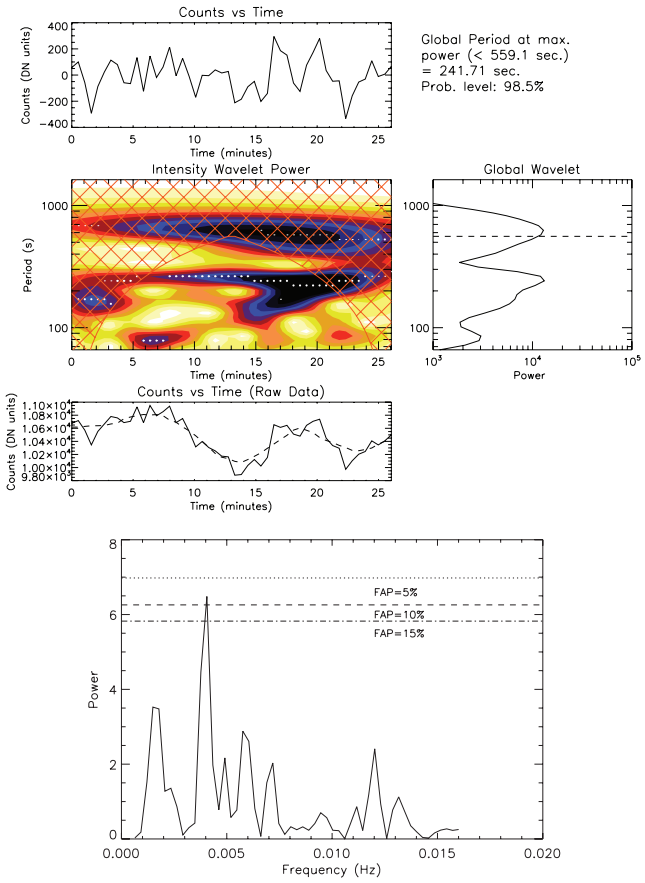

Figure 7. (a) The wavelet result for the Fe XII 195.12 Å EUV light curve. The top panel shows the variation of intensity. The wavelet power spectrum is given in the middle-left panel, and the global power spectrum is given in the middle-right panel with the dotted line showing the maximum allowable period outside the COI. The light curve is extracted from the core of the most brightened part of the BP (i.e. upper end of the flux-tube system). The brightest core of the BP is at $(X_\lambda, Y_{\rm SUN-OLD}) \sim$ [33.89th pixel, 339.04th pixel (or −142.711 arcsec)] as observed by the SW CCD independently. The same BP core is acquired at $(X_\lambda, Y_{\rm SUN-NEW}) \sim$ [33.89th pixel, 322.832th pixel (or −159.711 arcsec)] after its co-alignment with the He II 256.32 Å image as observed by the LW CCD. The light curve is detrended by a window width of 8 data points (i.e. ∼4.2 min) running average, which almost fit the long-term trend presented in the observed light curve. (b) The periodogram power spectrum of running average detrended light curve is presented in the bottom panel, which is consistent with the wavelet. The FAP levels are shown by horizontal lines.

wavelet and periodogram analyses on this detrended light curve, we obtain the statistically significant periodicity of 241 ± 60 s (around 5.0 min). We re-examine the obtained result using another method of wavelet reconstruction, which is found to be consistent with the previous result. However, we conclude that the trend removal by low-order polynomial fit is not appropriate as per the cyclic nature of the long-term trend presented in the Fe XII 195.12 Å EUV light curve.

The wavelet power transforms of the EUV light curves with cadence ∼32 s (see the top-left panels of Figs 6a and 7a) of He II 256 Å and Fe XII 195.12 Å are shown in the middle-left panels of Figs 6(a) and 7(a), where the darkest regions show the most enhanced oscillatory powers in the intensity wavelet spectrum. The cross-hatched areas are the COI, the region of the power spectrum where edge effects, because of the finite lengths of the time series, are likely to dominate. The maximum allowed period from the COI in all these wavelets, where the edge effect is more effective, is ∼559 s. In our wavelet analyses, we only consider the power peaks and corresponding real periods below this threshold. The periods with maximum power detectable outside the COI are ∼263 ± 80 s with a probability of ∼99–100 per cent and ∼ 241 ± 60 s with a probability of ∼98.5 per cent, respectively, in the lines He II 256 Å and Fe XII 195 Å. The approximate errors in the periodicities have been measured by FWHM estimation of power peaks in the global wavelet spectrum. The middle-right panels in Figs 6(a) and 7(a) show the global wavelet power spectra of these time series from which the statistically significant periods (i.e. centred at ∼263 and ∼241 s) are selected. It should be noted in the He II 256.32 Å intensity wavelet that the oscillatory period drifts between ∼220 and 290 s around the globally observed statistically significant period of ∼263 s. Similarly, in the Fe XII 195.12 Å intensity wavelet, the oscillatory period also drifts between ∼220 and 290 s around the globally observed statistically significant period of ∼241 s. We find the oscillation periods of ∼287 s (probability 99–100 per cent) and

∼241 s (probability 98 per cent), respectively, for the He II 256.32 Å and Fe XII 195.12 Å EUV light curves after removing jitters. However, we find that the periodicity ∼313 s (probability 96 per cent) in the Fe XV 284.16 Å EUV light curve changes to ∼143 s (probability 75 per cent) after removing the subarcsec EIS jitters, which is an artefact and insignificant.

We have also performed periodogram analyses (Scargle 1982) of the EUV light curves of He II 256 Å and Fe XII 195.12 Å (see Figs 6b and 7b). In the power spectra, the highest peak corresponds to the period of ∼270 s [false alarm probability (FAP) = 0.010] and ∼243 s (FAP = 0.080) for He II 256 Å and Fe XII 195 Å, respectively, which are consistent with those obtained from wavelet analysis. Therefore, the ∼5.0-min wavelet periods of He II 256 Å and Fe XII 195 Å appear to be statistically significant in our analysis. It should also be noted for the Fe XII 195.12 Å EUV light curve that the probability varies from 85 to 97 per cent with the change of the width of the running average window between '7' and '9'; however, the period remains the same (241 s). This is because these data are still dominated by the long-term periods around the COI, which causes an underestimation of the significance measurement by the randomization test for the power peak at the period 241 s below the COI. The nature of the long-term trends presented in Fe XII 195.12 Å is sinusoidal in nature and thus cannot be exactly fit with the low-order polynomial. Hence, we use an alternative method to re-examine our result as we obtained by wavelet and periodogram analyses of the running average subtracted Fe XII 195.12 Å EUV light curve. Hence, we use the wavelet reconstruction method of the raw light curve of Fe XII 195.12 Å to examine the existence of this power peak below the COI. The time series was reconstructed/filtered over all scale values corresponding to periods less than a period ∼443 s, which is below the COI period (559 s). We have selected the Fourier scale of 443 s, approximately 100 s below the COI period, in order to avoid the edge effect, as the region around the COI is full of unworthy long periods closely associated with this trend. This method confirms our previous argument that even below the COI there exists only the statistically significant period around 5.0 min. Hence, our decision to exactly fit and remove the long-term trend and associated period by running average (or low-order polynomial as in the case of He II 256.32 Å) is perfectly validated in our analyses. The extent of the COI at each period is the decorrelation time of the wavelet function. This is equal to $\sqrt{2}P$ for the Morlet wavelet function, where P is the oscillatory period. Our choice of the cut-off period (∼443 s) for the filtering was based on the value of the COI period (∼559 s) as longer periods cannot exist for a decorrelation duration outside the COI. In this test, the 241-s period exhibits a probability of 98 per cent. Hence, this test supports the existence of this period in the EUV light curve. Details of the wavelet reconstruction technique are given by Torrence & Compo (1998).

4 RESULTS AND DISCUSSION

An analysis of new observational data obtained by the EIS on board *Hinode* shows ∼263 ± 80 s and ∼241 ± 60 s intensity oscillations, respectively, in the He II 256.32 Å and Fe XII 195.12 Å EUV light curves, with a probability of >95 per cent above the BP close to the central disc. We also found the results derived from wavelets to be almost consistent with the results derived from their respective periodograms. The oscillations were observed independently in lines corresponding to different plasma temperatures: $\log T_{\rm He\,II} = 4.90$ and $\log T_{\rm Fe\,XII} = 6.20$. They lie near the powerful 5-min acoustic oscillations generated as a result of the subphotospheric convective motions. However, the lack of real intensity oscillations in the EUV light curve of Fe XV 284 Å formed at temperature $\log T_{\rm Fe\,XV} = 6.40$ rules out the possibility of the propagation of acoustic waves in the higher corona. These waves most likely cause the intensity oscillations in the He II 256.32 Å and Fe XII 195.12 Å EUV light curves. The oscillations are probably present at different heights, which implies that the wave propagates from the photosphere into the TR and the inner corona, but certainly not in the higher corona. As already noted, observed intensity oscillations in different EUV light curves over the BP may carry the signature of the propagation of ∼5-min acoustic oscillations from the photosphere upward.

Using *Transition Region and Coronal Explorer* (*TRACE*) 171-Å observations, de Moortel et al. (2002) have found the signature of acoustic oscillations with the period of 282 ± 93 s, which are excited near the loop footpoints and propagate in the lower part of these loops. McEwan & de Moortel (2006) have also found evidence of longitudinal oscillations of a number of loops in the lower corona with periods around ∼300 s. They have interpreted these as a leakage of 5-min p-mode oscillations upwardly in the outer atmosphere from near the footpoint of these loops. O'Shea et al. (2001) have also found a 5-min oscillation signature in an active region, which is commonly seen in TR (O V 629 Å) and coronal (Mg IX 368 and Fe XVI 335 Å) lines observed using the coronal diagnostic spectrometer (CDS) on board the Solar and Heliospheric Observatory (*SOHO*). They have interpreted it as a coupling of the photospheric acoustic driver with the longitudinal wave modes of TR and coronal loops. We also observed the intensity oscillations almost exactly in the same frequency range in the upper chromospheric (He II 256.32 Å) and inner coronal (Fe XII 195.12 Å) lines as observed by the *Hinode*/EIS. Hence, these observations may also be the most likely signature of acoustic wave propagation as per juxtaposition with these previously published results. Our observed frequencies are, however, below the photospheric cut-off value. These waves should not propagate upwards through the lower atmosphere for very long. Therefore, it is difficult to explain why they are observed in the upper atmosphere. An explanation can be found if the waves are generated *in situ*, or if they propagate at an arbitrary angle, which would reduce the cut-off frequency (De Pontieu, Erdélyi & James 2004). The BP system is probably made up of small-scale fine-structured loops as well as the tilted and expanding flux tubes (e.g. Péréz-Suárez et al. 2008; Jess et al. 2009). The small-scale and fine-structured loops are expected to be a subset of the tilted and expanding flux tubes related to the BPs. The co-aligned maps, as displayed in Fig. 5, provide clues for the presence of the small-scale loop system in the observed BP, which also seems to be an expanding flux tube from its footpoint to apex that fan out in the corona. These co-aligned images reveal the presence of a small-scale loop system, which is probably the subset of an expanding flux-tube system of the BP. The footpoint traces (or lower ends) of the flux-tube system lie in the chromosphere/TR, while its apex (or upper end) lies in the corona and is visible in coronal images. The maxima of the intensity contour is shifted in the BP system from upper chromosphere/TR to corona and is also spread over a large area. The upper part of the flux-tube system associated with the BP is visible in the high-temperature coronal lines (e.g. Fe XV 284.16 Å), while the root traces lie in the upper chromospheric/TR lines (e.g. He II 256 Å). The set of these maps does not provide the fine structure details associated with the BP. However, the presence of the expanding flux-tube system is evident. The choice of locations for deriving EUV light curves at different wavelengths to search for wave activity, probably present at different heights in the flux tubes, has been discussed in detail in Section 2. The *TRACE*

171-Å observations of slow waves in the lower part of the coronal loops also resemble the propagation of acoustic oscillations in the expanding flux tubes; however, at large scale. Hence, such expanding and pressure-balanced flux tubes at different length-scales may indeed offer the propagation of acoustic oscillations around the 5-min period in the lower solar atmosphere from the photosphere. The observed acoustic oscillations may propagate up to the inner corona through the flux-tube system of the BP in the reduced cut-off environment, as explained by De Pontieu et al. (2004). However, there is no clear signature of the tilt in the observed BP flux-tube system, so there is no direct evidence of the reduced cut-off environment above the BP as a result of tilt in the flux tube. Therefore, the most likely observational evidence of the finite radiative relaxation time in the plasma environment of the observed BP is evident. This may be a much more effective mechanism for reducing the acoustic cut-off frequency in the photosphere below the frequency related to ∼5-min periodicity and can compel the observed acoustic waves into the inner corona (e.g. Roberts 1983; Khomenko et al. 2008, and references therein). We do consider this mechanism as a most likely candidate for the transfer of 5.0-min acoustic wave energy from the photosphere to the inner corona above the observed BP.

We probably observe the dispersive acoustic oscillatory power in the upper chromosphere, which is amplified in the lower corona. The wavelet power spectrum and periodogram of the He II 256.32 Å light curve (cf. Figs 6a and b) show a ∼263-s periodicity, which is highly dispersive and clearly evident in the 'intensity versus time' panel of Fig. 6(a). The intensity wavelet of He II 256.32 Å exhibits a quasi-tadpole-like wavelet spectrum (cf. bottom-left panel of Fig. 6a). Nakariakov et al. (2004) have found real tadpole-like structures in their wavelet analyses, which can possibly be interpreted as fast MHD wave trains in the solar corona. The dispersion relation of the fast wave trains as described by Nakariakov et al. (2004) determines the shape of these real tadpole-like wavelet structures. That is, longer period wave trains travel faster and are eventually caught up away from the initiation site by the shorter period wave trains generated by the same impulse in the solar corona. We use the term 'quasi-tadpole' in our case because the observed intensity wavelet spectra of He II 256 Å and Fe XII 195 Å show the period drift towards shorter periods. However, they do not display the same tadpole heads associated with the continuation of wave power at longer periods simultaneous with the addition of shorter-period power. Hence, these tadpole-like structures only show the drift of continuous power from the longer period associated with the thick power head to the shorter period associated with the narrow power tail. Therefore, they are 'quasi' in nature (i.e. they seem to be tadpole but not like the real tadpoles as observed by Nakariakov et al. 2004 associated with the fast MHD wave trains). In the intensity wavelet spectra shown in Figs 6(a) and 7(a), the clearly visible quasi-tadpole-like structures show a reversal in their power distribution. The power is stronger at the beginning of the total span of observation in the intensity wavelet of He II 256.32 Å while it becomes greater at the end of the total observation period in the intensity wavelet of Fe XII 195 Å. This may be a most likely signature of the amplification of observed intensity (thus acoustic) oscillations in the corona, after its dispersion in the upper chromosphere/TR. In this scenario, the photospherically generated acoustic oscillatory power around the ∼5.0-min periodicity may propagate through the upper chromosphere/TR where the He II 256.32 Å line is formed and generate intensity oscillations with the damping of oscillation power (cf. top-left and bottom-left panels of Fig. 6a). However, such oscillations are also observed in the Fe XII 195.12 Å line in the inner corona with slight amplifications in the intensity oscillatory pattern and thus the associated powers (cf. top-left and bottom-left panels of Fig. 7a). However, no evidence of amplified oscillations around ∼5-min real oscillations occurs in the higher corona where the Fe XV 284.16 Å line is formed, which rules out this type of mode coupling there. In the intensity wavelet spectra of He II 256 Å, the oscillatory power becomes weaker during the total span of observations. This is also an indicator of the temporal damping of the acoustic waves in the upper chromosphere/TR as a result of non-ideal MHD effects (e.g. thermal conduction, radiative cooling). The radiative cooling causes the temporal decrement of sound speed in the upper chromospheric/TR part of the BP. If we consider the formation of the BP by small-scale loop/expanding flux-tube systems as evident in Fig. 5, then this effect prolongs the oscillation period P inversely proportional to the decreasing sound speed (C_s), which has not yet been tested observationally (Aschwanden 2004). The quasi-tadpole of the He II 256.32 Å intensity wavelet shows approximately linear decrement and drift over the total lifespan of the time series. Therefore, this quasi-tadpole drift may be a result of the above-mentioned radiative cooling and related acoustic damping in the upper chromosphere/TR region above the BP system. Recently, a detailed theoretical study has also been carried out by Morton, Hood & Erdélyi (2010) to study the effect of cooling in an homogeneous solar plasma on the properties of propagating MHD waves. Morton & Erdélyi (2009) have also carried out the first detailed theoretical study of the effect of cooling on the oscillation properties of the transverse MHD waves.

The difference between the tadpole structure seen by Nakariakov et al. (2004) and the present structure seen in the He II 256.32 Å intensity wavelet might be a result of more evolved effects of dispersion because of radiative cooling. The dispersion may cause a longer time delay between longer- and shorter-period wave packets, which may never arrive at the same time in a particular layer. This also confirms that the finite radiative relaxation time also supports the formation of a reduced cut-off environment above the BP, which forces the acoustic oscillations up to the inner corona. Hence, we probably obtain the first most likely observational signature of the oscillation period drift because of radiative cooling. Therefore, radiative cooling may be the most effective dissipation mechanism, and the finite radiative relaxation time may be the efficient driver of 5.0-min acoustic oscillations in the small-scale BP system. However, we cannot rule out the possibility of other dissipative mechanisms in the same region.

The signature of self-consistent growth of acoustic oscillations in the dispersive inner corona is difficult to explain, as it has already been dissipated to some extent in the upper chromosphere/TR. This probably indicates that there is yet another indirect mechanism that is forcing the acoustic oscillations *in situ* from the upper chromosphere to the lower corona, and imposed over the continuous leakage of dispersive acoustic oscillations as a result of the radiative cooling from the upper chromosphere/TR into the inner corona. Our observations, which show the self-consistent growth of acoustic oscillations in the inner corona, probably reveal the most likely signature of two-wave MHD interactions (mode coupling) when the acoustic oscillations pass through the lower solar atmosphere (i.e. upper chromosphere where He II 256.32 Å is formed) to the inner corona (where the Fe XII 195.12 Å line is formed) between which probably the plasma beta approaches unity. Zaqarashvili et al. (2006) have shown that the resonant energy conversion from Alfvén to acoustic waves occurs near the region where the plasma beta

approaches unity (or more precisely, where the ratio of sound to Alfvén speeds approaches unity) probably in the inner corona. Similarly, Ulmschneider, Zahringer & Musielak (1991) have also studied the non-linear two-wave interaction of the longitudinal waves with the transversal waves of the double period in the magnetic flux tubes. We observe the acoustic oscillations around 5.0 min between the upper chromosphere and corona. Therefore, in principle, the Alfvén oscillations of double period (i.e. ∼10 min) may resonantly amplify the highly dispersive acoustic oscillations when it passes through the inner corona, as theorized by Zaqarashvili et al. (2006) and Ulmschneider et al. (1991). These most probable periods of Alfvén oscillations, which can resonantly transfer the energy to our observed acoustic oscillations, lie in the family of first observed Alfvén waves with period less than <700 s (∼12 min; Jess et al. 2009) above the BPs. However, there is no direct evidence of Alfvén waves of ∼10-min periodicity in our observations. McAteer et al. (2003) have also found the signature of such a type of mode coupling in the network BP that lies in the chromosphere. Moreover, we notice a very interesting phenomenon by the intensity wavelet of the inner coronal line Fe XII 195.12 Å along the full length of its exhibited 'quasi-tadpole'. The decreasing and increasing trends of the period drift are also evident in this intensity wavelet of Fe XII 195.12 Å, which may also be the most likely signature of ongoing cooling (probably as a result of radiative cooling) and heating (probably as a result of resonant energy transfer by Alfvén waves) of the plasma in the BP. The increasing trend of the period drift is clearly presented at the scale near to ∼10 min, which may be the most likely confirmatory signature of the resonant transfer of energy from the transversal wave of double period (∼10 min) to the dispersed acoustic oscillations around ∼5.0 min. The first detailed theoretical models have been reported by Morton & Erdelyi (2009) and Morton et al. (2010) to study such effects of radiative cooling on the various MHD modes/waves in the coronal loops. The detailed theoretical studies of such effects on MHD waves in the small-scale structures (e.g. our observed BP) are still open.

In conclusion, we report on the transfer of the ∼5.0-min acoustic wave energy via the reduced cut-off environment above the observed BP as a result of the effect of the finite radiative relaxation time. We probably find the first observational signature of the radiative cooling as one of the efficient damping mechanisms for the acoustic oscillations in the chromospheric part of the BP system, which is also responsible for the period drift of the 5.0-min acoustic oscillations during the total span of the observations. We also explain the amplification of the ∼5.0-min acoustic oscillation power in the inner corona as a most likely response of two-wave MHD interactions (MHD mode coupling) above the BP under the observational baseline of this particular *Hinode*/EIS data set. We describe this evidence of wave coupling of acoustic oscillations as most expected Alfvén waves of double periodicity above the EUV BP. However, we take into account the indirect evidence of these waves with period ∼700 s recently observed above the BPs (Jess et al. 2009). This indirect but most likely signature of wave coupling may be crucial to understanding the wave dynamics above the EUV BPs, noting that such observations of wave coupling have already been reported in the cool and low-lying counterpart of chromospheric network BPs (McAteer et al. 2003). High-cadence spectral and imaging observations can shed light on the simultaneous presence of the transversal wave above the BP. Therefore, future detailed observational searches should be carried out, especially using both ground-based and space-based high cadence imaging and spectroscopy, to find the simultaneous presence of transverse and acoustic oscillations in the solar atmosphere locally in order to study their coupling more precisely.

ACKNOWLEDGMENTS

We wish to express our gratitude to the referee for valuable comments, which improved the manuscript considerably. AKS wishes to express his gratitude to Dr E. O'Shea for providing the RANDOMLET tool, and to Professor R. Sagar for valuable discussions. AKS also acknowledges the support of a joint DST-RFBR project grant (INT/RFBR/P-38) for the research work. We acknowledge the observing sequence of Hansteen, Antolin and Arikawa, which is available in the EIS-Data base at MSSL, UK *Hinode*/EIS website. *Hinode* is a Japanese mission developed and launched by Institute of Space and Astronautical Science (ISAS)/Japan Space Exploration Agency (JAXA), with the National Astronomical Observatory of Japan (NAOJ) as a domestic partner and the National Aeronautics and Space Administration (NASA) and the Science and Technology Facilities Council (STFC, UK) as international partners. It is operated by these agencies in cooperation with the European Space Agency (ESA) and the Norwegian Space Centre (NSC, Norway).

REFERENCES

Aschwanden M. J., 2004, Physics of the Solar Corona. Springer, Berlin
Cirtain J. W. et al., 2007, Sci, 318, 1580
Culhane J. L. et al., 2006, Proc. SPIE, 6266, 22
de Moortel I., Ireland J., Hood A. W., Walsh R. W., 2002, A&A, 387, L13
De Pontieu B., Erdélyi R., James S. P., 2004, Nat, 430, 536
De Pontieu B. et al., 2007, Sci, 318, 1574
Dwivedi B. N., Srivastava A. K., 2006, SoPh, 243, 153
Dwivedi B. N., Srivastava A. K., 2008, NewA, 13, 581
Erdélyi R., Fedun V., 2007, Sci, 318, 1572
Erdélyi R., Taroyan Y., 2008, A&A, 489, L49
Fossum A., Carlsson M., 2005, Nat, 435, 919
Gruszecki M., Murawski K., Ofman L., 2008, A&A, 488, 757
Gupta A. C., Srivastava A. K., Wiita P. J., 2009, ApJ, 690, 216
Jess D. B., Mathioudakis M., Erdélyi R., Crockett P. J., Keenan F. P., Christian D. J., 2009, Sci, 323, 1582
Khomenko E., Centeno R., Collados M., Trujillo Bueno J., 2008, ApJ, 676, L85
Linnell-Nemec A. F., Nemec J. M., 1985, AJ, 90, 2317
McAteer R. T. Z., Gallagher P. T., Williams D. R., Mathioudakis M., Bloomfield D. S., Phillips K. J. H., Keenan F. P., 2003, ApJ, 587, 806
McEwan M. P., de Moortel I., 2006, A&A, 448, 763
Morton R. J., Erdélyi R., 2009, ApJ, 707, 750
Morton R. J., Hood A. W., Erdélyi R., 2010, A&A, 512, 23
Nakariakov V. M., Arber T. D., Ault C. E., Katsiyannis A. C., Williams D. R., Keenan F. P., 2004, MNRAS, 349, 705
Ofman L., Wang T. J., 2008, A&A, 482, L9
Okamoto T. J. et al., 2007, Sci, 318, 1577
O'Shea E., Doyle J. G., 2009, A&A, 494, 355
O'Shea E., Banerjee D., Doyle J. G., Fleck B., Murtagh F., 2001, A&A, 368, 1095
O'Shea E., Srivastava A. K., Doyle J. G., Banerjee D., 2007, A&A, 473, L13
Pandey J. C., Srivastava A. K., 2009, ApJ, 697, L153
Péréz-Suárez D., Maclean R. C., Doyle J. G., Madjarska M. S., 2008, A&A, 492, 575
Roberts B., 1983, Sol. Phys., 87, 77
Scargle J. D., 1982, ApJ, 263, 835
Srivastava A. K., 2010, NewA, doi:10.1016/j.newast.2010.02.006
Srivastava A. K., Dwivedi B. N., 2010, NewA, 15, 8

Srivastava A. K., Zaqarashvili T. V., Uddin W., Dwivedi B. N., Kumar P., 2008a, MNRAS, 388, 1899
Srivastava A. K., Kuridze D., Zaqarashvili T. V., Dwivedi B. N., 2008b, A&A, 481, L95
Tomczyk S., McIntosh S. W., Keil S. L., Judge P. G., Schad T., Seeley D. H., Edmondson J., 2007, Sci, 317, 1192
Torrence C., Compo G. P., 1998, BAMS, 79, 61
Ulmschneider P., Zahringer K., Musielak Z. E., 1991, A&A, 241, 625
van Doorsselaere T., Nakariakov V. M., Verwichte E., 2008, ApJ, 676, L73
Vasheghani Farahani S., van Doorsselaere T., Verwichte E., Nakariakov V. M., 2009, A&A, 498, L29
Wang T. J., Ofman L., Davila J. M., 2009, ApJ, 696, 1448
Zaqarashvili T. V., Roberts B., 2006, A&A, 452, 1053
Zaqarashvili T. V., Oliver R., Ballester J. L., 2006, A&A, 456, L13

This paper has been typeset from a TEX/LATEX file prepared by the author.